

Andersson-Magnéli Phases Ti_nO_{2n-1} : Recent Progress Inspired by Swedish Scientists

Qing Zhang^{+,*^[a]} Weiyan Liu^{+,^[a]} Yi Zhou,^[a] Junyan Li,^[a] Tu Sun,^[a] Qingyuan Liu,^[b] Yanhang Ma,^{*^[a]} Jinghui Wang,^[a] Jun Li,^[a] Ruoshi Zhao,^[c] Yu Sui,^[b] Takashi Matsumoto,^[d] Norihiro Muroyama,^[d] Akihito Yamano,^[d] Kenneth D. M. Harris,^{*^[e]} Zhijian James Shen,^[c, f] and Osamu Terasaki^{*^[a]}

Dedicated to Professor Sven Lidin on the occasion of his 60th birthday.

Among homologous series of metal oxides, Andersson-Magnéli phases Ti_nO_{2n-1} ($n=4-10$) have attracted renewed scientific attention because of their behaviour in electrical conductivity and chemical/thermal stability. Various applications have also been reported for the phases with different values of n , or slightly reduced rutile (TiO_2). The characteristic properties of these materials depend strongly on the compositional deviation from TiO_2 and the way in which the structure accommodates the deviation. Thus, an urgent requirement is to overcome difficulties in characterizing such materials at atomic resolution. Here, we trace the discovery of the Andersson-Magnéli phases, and report the application of recent developments in electron

microscopy to reveal the relation, at the local level, between structural characteristics and electronic states, specifically for the materials Ti_nO_{2n-1} with $n=4-8$. The electrical conductivity of Ti_4O_7 has been reported previously to show three clearly distinct states on decreasing temperature from 300 K. For this reason, we focus on Ti_4O_7 as a representative example of the Ti_nO_{2n-1} phases and report structural characteristics at temperatures corresponding to each of the three different phases, focusing on the distribution of Ti^{3+} and Ti^{4+} cations from analysis of single-crystal XRD data. Electron diffraction experiments and electrical conductivity measurements are also reported.

Introduction

There is no doubt that precise and reproducible experiments resulting from instrumental developments, creative ideas and the combined application of multi-technique strategies have shaped the development of the field of Solid-State Chemistry. In the 1950s, scientific efforts were focused on understanding the role of defects from perfect crystalline order in controlling the properties of materials. Extensive efforts were made to characterize defects, including point, linear, planar and ex-

tended defects. Driven by the preparation of high-purity metals for Fermiology and of thin crystal films, transmission electron microscopy (TEM) was developed, both in experimental and theoretical aspects, to characterize impurities, dislocations and stacking faults in Europe, especially in the U.K.^[1] In Solid-State Chemistry, many transition metal oxides or chalcogenides showing very high “apparent” point-defect concentrations were discovered and synthesized. Developing realistic structural models to explain the unusual stoichiometries of these materials became a hot scientific topic, either by introducing

[a] Dr. Q. Zhang,⁺ W. Liu,⁺ Dr. Y. Zhou, J. Li, T. Sun, Prof. Y. Ma, Dr. J. Wang, Prof. J. Li, Prof. O. Terasaki
School of Physical Science and Technology
ShanghaiTech University
Shanghai, China
E-mail: zhangqing1@shanghaitech.edu.cn
mayh2@shanghaitech.edu.cn
osamuterasaki@mac.com

[b] Q. Liu, Prof. Y. Sui
School of Physics
Harbin Institute of Technology
Harbin, China

[c] R. Zhao, Prof. Z. J. Shen
School of Materials Science and Engineering
Tsinghua University
Beijing, China

[d] Dr. T. Matsumoto, Dr. N. Muroyama, Dr. A. Yamano
X-ray Instrument Division
Rigaku Corporation
Tokyo 196-8666, Japan

[e] Prof. K. D. M. Harris
School of Chemistry
Cardiff University
Cardiff CF10 3AT, U.K.
E-mail: HarrisKDM@cardiff.ac.uk

[f] Prof. Z. J. Shen
Department of Materials and Environmental Chemistry
Stockholm University
Stockholm SE-10691, Sweden

[⁺] These authors contributed equally to this work.

 Supporting information for this article is available on the WWW under <https://doi.org/10.1002/zaac.202000408>

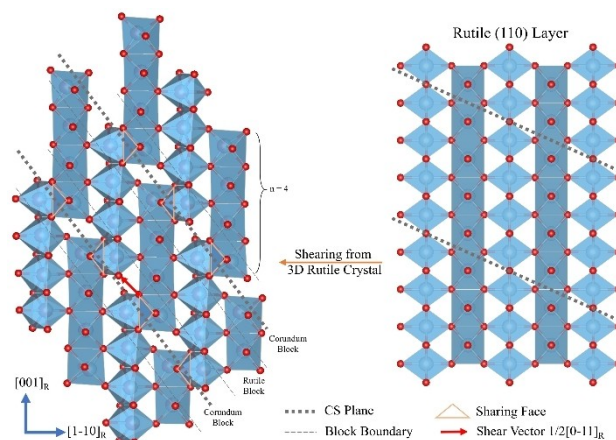
 © 2020 The Authors. *Zeitschrift für anorganische und allgemeine Chemie* published by Wiley-VCH GmbH. This is an open access article under the terms of the Creative Commons Attribution Non-Commercial NoDerivs License, which permits use and distribution in any medium, provided the original work is properly cited, the use is non-commercial and no modifications or adaptations are made.

point defects to retain simple structures such as rock-salt and fluorite types, or by modification or reorganization of the host crystal structure.^[2] In this respect, understanding structural characteristics of the TiO_x system is a fertile research target, as this system covers both of these cases in different composition regimes of TiO_x .

Concerning precise experiments at that time, Gunnar Hägg had designed the Guinier-Hägg powder X-ray focusing camera with a quartz monochromator prepared in his laboratory. The camera was an extremely powerful, precise and rather simple instrument.^[3] He also built the first Weissenberg camera in Sweden for single-crystal XRD measurements.^[4] In keeping with Hägg's style for science based on precise measurements with an open, fair and creative mind, Arne Magnéli, Sten Andersson and Lars Kihlberg followed in his footsteps and contributed greatly to the topic of homologous series of phases and Solid-State Chemistry. Sven Lidin was their successor in Stockholm University and is further extending their spirit in the international arena.

The Guinier-Hägg camera played an important role in structural analysis of TiO_x systems, yielding structure determination of several materials from powder samples,^[5] showing that: (a) the NaCl structure type exists for a wide range of compositions ($0.64 \leq x \leq 1.25$) at high temperature, and (b) the homologous series of phases formulated as $\text{Ti}_n\text{O}_{2n-1}$ ($n=4-10$) exists for TiO_x with $1.75 \leq x \leq 1.9$.^[2] Using data from the Weissenberg camera, Sten Andersson solved the structure of Ti_5O_9 from a single crystalline fragment obtained by crushing a crystal with a relatively small twin parasite. He established the general principle for the Andersson-Magnéli phases $\text{Ti}_n\text{O}_{2n-1}$ ($n=4-10$), which deviate slightly from TiO_2 and Ti_2O_3 by the introduction of crystallographic shear (CS) parallel to $(121)_R$ with the shear vector $1/2[0-11]_R$ periodically into the rutile structure of TiO_2 .^[6] Although these materials are generally referred to as Magnéli phases, we prefer to use the term Andersson-Magnéli phases, recognizing the critical contributions made by Sten Andersson in establishing the structural characteristics of these materials. Throughout this paper, subscripts R and M denote, respectively, indices based on the rutile structure and the Andersson-Magnéli phase; Scheme 1. These structures contain adjacent rutile-type chains comprising a number (n) of edge-sharing TiO_6 octahedra running along the $[001]_R$ axis, with the octahedra at each end of the chains sharing faces with the next chain, as in Ti_2O_3 . A primitive study of the structure and manner of coexistence of neighbouring n -phases in $\text{Ti}_n\text{O}_{2n-1}$ ($n=4-10$) was reported by one of us 50 years ago using transmission electron microscopy (TEM); at that time, the spatial resolution of TEM was *ca.* 4.0 Å.^[7] We note that rutile (TiO_2) and Ti_2O_3 are not the end-members of this family of materials, and the existence of another series with the same formula $\text{Ti}_n\text{O}_{2n-1}$ ($15 \leq n \leq 39$) but with oxygen vacancies arranged in the $(132)_R$ shear plane [rather than $(121)_R$] is observed for TiO_x with $1.933 \leq x \leq 1.972$.^[8]

By fixing the electronic state of oxygen as O^{2-} , these materials have been discussed as mixed valence compounds containing, per formula unit, 2 Ti^{3+} ions (electronic configuration $3d^1$) and $(n-2)$ Ti^{4+} ions (electronic configuration $3d^0$).



Scheme 1. The crystal structure of the Andersson-Magnéli phase Ti_4O_7 , shown on the left, can be considered to be derived from the structure of rutile TiO_2 (one layer of which, perpendicular to $[110]_R$, is shown on the right). The Ti_4O_7 structure is derived from rutile by crystallographic shear of the $(121)_R$ plane with $1/2[0-11]_R$ vector (red arrow) every four octahedra from rutile. A corundum-like structure appears near the shear planes with face-sharing octahedra, denoted as “corundum block”.

Transport properties of Andersson-Magnéli phases $\text{Ti}_n\text{O}_{2n-1}$ ($n=4-10$) have been discussed as strongly dependent on non-stoichiometry, with point defects or planar defects. Physical properties of $\text{Ti}_n\text{O}_{2n-1}$ ($n=4-10$) materials, such as electrical conductivity and magnetic susceptibility, have attracted great interest from the early studies (together with another isostructural Andersson-Magnéli phase $\text{V}_n\text{O}_{2n-1}$) because they show drastic changes with temperature in a cooperative fashion to structural transitions. These transitions have been used to check sample purity and, more fundamentally, have been interpreted in terms of the localization of electrons in the cation sublattice and the charge distribution at cation sites, corresponding to various charge-ordered states.

Electron microscopy is a unique approach in providing (in principle) correlative information from a given nano-region of a material in real space (structure), momentum space (diffraction/spatial-correlation) and energy space (electronic state) as a function of atomic positions. Given the enormous recent developments in high-resolution scanning transmission electron microscopy (STEM), we now have an ideal opportunity to observe, in unprecedented detail, the structures and electronic states of specific local areas of the Andersson-Magnéli phases $\text{Ti}_n\text{O}_{2n-1}$.

One of the Andersson-Magnéli phases, Ti_4O_7 , has been studied with particular intensity, starting from structural aspects.^[9,10] Marezio *et al.*^[11] investigated structural phase transitions of Ti_4O_7 from single-crystal XRD data recorded at three different temperatures (298 K, 140 K, 120 K). Based on measured bond distances, they discussed the electronic states of Ti^{3+} or Ti^{4+} cations, their locations and physical properties. At 298 K, Ti_4O_7 was assigned as a metallic state, with Ti^{3+} and Ti^{4+} cations arranged randomly to give an average valence of 3.5 for each Ti

site. At 120 K, the material was assigned as an insulator and non-magnetic, with Ti^{3+} and Ti^{4+} ions arranged in an ordered fashion to form a $\text{Ti}^{3+}\text{-Ti}^{3+}$ pair. In the intermediate state at 140 K, there was no indication of charge separation, and it was speculated that local charge separation and pair bonding exists, with no long-range order of this bonding arrangement. However, Marezio *et al.* did not discuss the electronic distribution within the unit cell, perhaps as a limitation of the small number of reflections observed in their single-crystal XRD data. From photoemission spectroscopy, the electronic states of Ti_4O_7 have been discussed in terms of two-step transitions from a metallic state to a bipolaronic insulator,^[12] with a metallic Fermi edge in the room temperature phase, with a gap of *ca.* 100 meV in the insulating state, and with a pseudo-gap feature in the intermediate phase.^[13] Furthermore, superconductivity has been observed in an epitaxially grown thin film of Ti_4O_7 on Al_2O_3 , which may be induced by oxygen deficiency and epitaxial stabilization.^[14]

Recently one of us (Y. Sui) has succeeded in synthesizing a high-quality single crystal of Ti_4O_7 and has measured electrical conductivity along three principal axes in the temperature range from 50 K to 250 K, with abrupt changes observed at 154 K and 110 K.^[15]

Inspired by the pioneering work of Swedish scientists (discussed above) in the structural characterization of Andersson-Magnéli phases, we report recent progress in understanding the properties of these materials through the combined application of a range of state-of-the-art experimental methodologies. In particular, by taking advantage of recent developments in electron microscopy to reveal the relation between local structural characteristics and electronic states, we report a comprehensive characterization of several members of the Andersson-Magnéli phases $\text{Ti}_n\text{O}_{2n-1}$ ($n=4-8$) using frontier electron microscopy techniques. In parallel, facilitated by the availability of high-quality single crystals of Ti_4O_7 , we also focus on a multi-technique investigation of the structural characteristics and phase transitions in this specific material from high-quality single-crystal XRD data and 3D electron diffraction data, as well as measurements of electrical conductivity and magnetic susceptibility.

Results and Discussion

[I] Study of $\text{Ti}_n\text{O}_{2n-1}$ ($n=4-8$) Materials by Electron Microscopy

We have characterized the structures of the Andersson-Magnéli phases $\text{Ti}_n\text{O}_{2n-1}$ ($n=4-8$) from three different samples (single crystals of Ti_4O_7 , and bulk samples 1 and 2 (see Figure 1(a)) using HR-STEM with spherical aberration (Cs) correctors. All Ti and O atoms are observed clearly (see Figure 2, as discussed in detail below), including details of the CS planes. The electronic states of the Ti atoms have been probed by electron energy loss spectroscopy (EELS) using the recently developed direct detection technique in counting EELS mode, which provides a

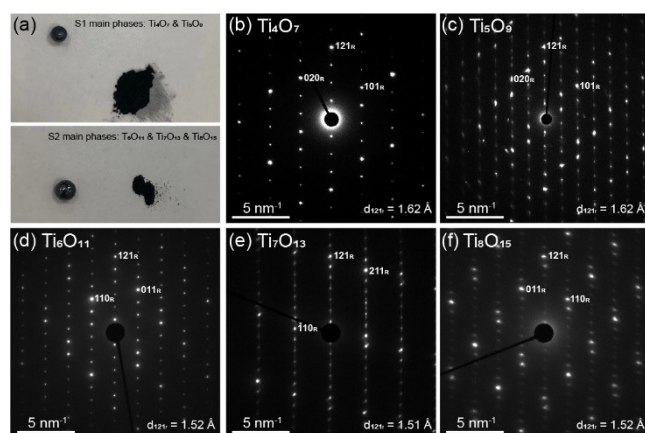


Figure 1. (a) The original bulk samples 1 and 2 (denoted S1 and S2), which were crushed into fine powders for S/TEM observations. (b–f) SAED patterns of $\text{Ti}_n\text{O}_{2n-1}$ with $n=4-8$. Indices refer to the 121_R reflection of rutile, TiO_2 .

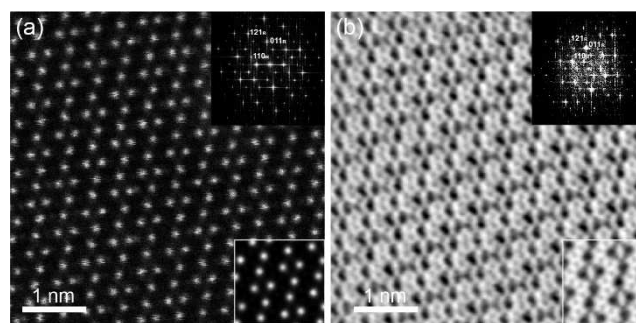


Figure 2. HR-STEM images of Ti_4O_7 along the $[1-11]_R$ zone axis, collected on GrandARM 300F with 300 kV accelerating voltage, together with Fourier diffractograms from the images (top right) and simulated images (bottom right), respectively: (a) HAADF image, and (b) enhanced ADF image by using segmented annular all field detector.

potential approach to deeply understand the bonding states of these materials at the atomic level.

Selected area electron diffraction (SAED) patterns for sample 1 and sample 2 give information on the composition n in $\text{Ti}_n\text{O}_{2n-1}$ ($n=4-8$) and the CS planes. The shear vector^[7] is clearly identified from the $(n-1)$ equally spaced spots between the origin and the strong reflections corresponding to $(121)_R$, as shown in Figure 1(b–f), which is consistent with powder XRD results (Figure S1). High-quality HR-TEM images have been recorded for Ti_4O_7 ,^[16,17] Ti_6O_{11} ^[18] and Ti_8O_{17} .^[17] However, from the HR-TEM images, specifying the Ti and O atoms including defects with atomic resolution in the regions near the CS planes remains challenging. Using a spherical aberration (Cs) corrected transmission electron microscope in combination with high-angle annular dark field (HAADF) detector and enhanced annular bright field (eABF) detectors, we report for the first-time high-resolution STEM images of Ti_4O_7 , in which all Ti and O

atoms are observed clearly, especially in the regions near the CS planes.

In STEM mode, the contrast of HAADF images is proportional to $Z^{1.4-2}$ (Z-contrast), where Z is the atomic number of the components. Therefore, HAADF images show much stronger contrast for Ti atoms than O atoms, and the contrast of light O atoms is hard to observe. The HAADF-STEM image taken along the $[1-11]_R$ zone axis in rutile shows clearly the CS planes parallel to $(121)_R$ in Ti_4O_7 (Figure 2a). The period of the CS planes is determined to be 6.5 Å for Ti_4O_7 ; all Ti atoms are resolved and their positions match well with the simulated STEM image (bottom right in Figure 2a). In order to observe the O atoms, we used enhanced ABF (eABF) imaging by taking the difference between the ABF image and the corresponding BF image captured simultaneously by an eight-segmented annular all-field detector (SAAF). As shown in Figure 2b, all O atoms, including the vacancies at the CS planes, are in good agreement with the simulated STEM image (bottom right). In addition, as shown in Figure 3, extra contrast spots (highlighted by yellow arrows) appear in the CS plane region in both HAADF and eABF images, which we attribute as a consequence of electron beam interaction with the material. The structural evolution in the region of the shear planes resulting from this effect requires more detailed investigation, and will be the focus of future studies.

In addition to atomic-resolution STEM images, we measured electron energy loss spectroscopy (EELS) data to investigate the valence state of Ti, using a newly developed technology combining direct detection in counting mode and Quantum EELS. The best energy resolution to characterize the energy loss near edge structure (ELNES) with extremely low electron dose (e.g. down to 10 e^- /pixel/s) is achieved with minimum electron beam damage on the sample.

Ti $L_{3,2}$ ELNES spectra of Andersson-Magnéli phases, studied by Stoyanov since 2007,^[19] have been shown to contain mainly four white lines that are clearly resolved in TiO_2 (with Ti in the Ti^{4+} state), while the pre-peaks of Ti^{3+} in Ti_2O_3 are much weaker. However, EELS spectra recorded in TEM mode may include signal from e-beam damaged areas. Therefore, within a small area under STEM mode (Figure S3), we measured ELNES data on pure TiO_2 and Ti_2O_3 crystals as standards under the same experimental conditions as the Andersson-Magnéli phase Ti_8O_{15} . With large n , the rutile-like structure covers a wider range

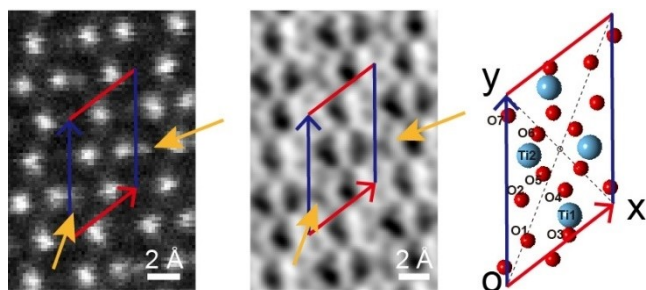


Figure 3. Extra contrast, marked with yellow arrows, in HAADF and eABF-STEM images for Ti_4O_7 .

leading to fewer e -beam sensitive areas and more convincing spectral data. As shown in Figure 4, the Ti L_2 and Ti L_3 pre-peaks for Ti_8O_{15} are between those of Ti^{4+} in TiO_2 and Ti^{3+} in Ti_2O_3 . Thus, we believe that the observed valence states of Ti in the Andersson-Magnéli phase are real, rather than a consequence of e -beam damage. However, due to beam sensitivity in the region of the CS plane, the exposure time of the EELS measurement was not long enough to give high SNR; as a result, it is challenging to obtain an atomic resolution spectral image that would allow the valence state of each Ti site to be established.

[[I]] Crystal Structure of Ti_4O_7

(a) Single-crystal XRD: High-quality single-crystal XRD data were recorded for Ti_4O_7 at 298 K, 145 K and 98 K, corresponding to the three different phases discussed above. In our analysis of the data, our description of the structure is based on the primitive triclinic system (space group $P\bar{1}$), which is equivalent to the description (based on space group $A\bar{1}$ with doubled unit cell volume) of Marezio *et al.*^[11] There are small (but significant) differences in the unit cell parameters determined at each temperature, and there is a slight increase in the unit cell volume in the low temperature phases (Table 1). Initially, structure determination was based on the use of X-ray scattering factors for neutral Ti and O atoms, with structure solution carried out by *SHELXT*^[20] using the intrinsic phasing method and with structure refinement carried out by *SHELXL*^[21] using least-squares minimization in *Olex2*.^[22] The refined structure shows the characteristic features of the Andersson-Magnéli phase Ti_4O_7 , with chains of edge-sharing TiO_6 octahedra truncated every four octahedra by the crystallographic shear planes. The average Ti–O bond lengths for the four independent Ti sites are in good agreement with those reported by Marezio *et al.*^[11] at the different temperatures studied, although the higher quality of single-crystal XRD data used in the present work leads to significantly greater accuracy in the geometric details of the crystal structure. For example, the esds in the Ti–O bond lengths in the refined structures of

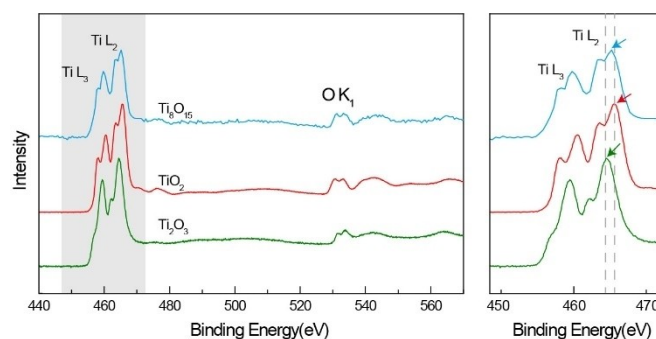


Figure 4. EEL spectra of Ti_2O_3 (green), TiO_2 (red) and Ti_8O_{15} (blue), in which separate Ti^{3+} and Ti^{4+} L-edges are observed. Grey dashed lines and arrows mark the relative positions of the d peak^[19] of the L_2 edge of Ti_2O_3 (Ti^{3+}), TiO_2 (Ti^{4+}) and Ti_8O_{15} .

Table 1. Crystallographic data for Ti_4O_7 at different temperatures, with structure solution and refinement carried out using X-ray scattering factors for neutral atoms.

T/K	298	145	98
Space group	$P\bar{1}$	$P\bar{1}$	$P\bar{1}$
a/Å	5.59836(11)	5.59699(9)	5.62446(6)
b/Å	6.90288(13)	6.91907(8)	6.89093(7)
c/Å	7.12445(10)	7.13403(11)	7.20029(7)
$\alpha/^\circ$	64.1233(16)	64.0851(13)	63.7174(10)
$\beta/^\circ$	71.1956(15)	70.9808(14)	70.3532(9)
$\gamma/^\circ$	75.5935(16)	75.3230(11)	74.7688(9)
V/Å ³	232.599(8)	232.918(6)	233.499(5)
Radiation	Mo K α ($\lambda = 0.71073$ Å)	Mo K α ($\lambda = 0.71073$ Å)	Mo K α ($\lambda = 0.71073$ Å)
Reflections collected	76961	66551	65672
Independent reflections	7593 $R_{\text{int}} = 0.0313$ $R_{\text{sigma}} = 0.0160$	7606 $R_{\text{int}} = 0.0488$ $R_{\text{sigma}} = 0.0286$	7612 $R_{\text{int}} = 0.0384$ $R_{\text{sigma}} = 0.0208$
GOF on F ²	1.077	1.021	1.121
Final R indices	$R_1 = 0.0175$ $wR_2 = 0.0337$	$R_1 = 0.0233$ $wR_2 = 0.0471$	$R_1 = 0.0155$ $wR_2 = 0.0336$
$I \geq 2\sigma(I)$			
Final R indices	$R_1 = 0.0292$ $wR_2 = 0.0411$	$R_1 = 0.0407$ $wR_2 = 0.0517$	$R_1 = 0.0201$ $wR_2 = 0.0412$
[all data]			

Marezio *et al.*^[11] (considering all temperatures studied) are in the range 0.002–0.004 Å, whereas the esds in the Ti–O bond lengths in our refined structures (considering all temperatures studied) are in the range 0.0003–0.0005 Å.

By analysis of the Ti–O bond lengths and distances between Ti sites, Marezio *et al.*^[23] rationalized the phase transition and physical properties of Ti_4O_7 in terms of order/disorder in the distribution of the Ti^{3+} and Ti^{4+} cations in the structure. They proposed that, in the high-temperature phase, the Ti^{3+} and Ti^{4+} cations are distributed with random disorder in each Ti site, whereas in the low-temperature phase, the Ti^{3+} cations are located on two sites to form pairs (bipolaron). The same conclusion can be reached by interpreting our results at the same level, based simply on consideration of the interatomic distances.

However, consideration of the real space electron distribution is a more direct and powerful approach for determining the charge distribution or cation valence. With the state-of-the-art Rigaku instrument used to record the single-crystal XRD data in the present work, about 20 times more reflections were measured in our data collections for Ti_4O_7 than in the measurements of Marezio *et al.*^[11,23] allowing a more precise, high-resolution determination of the electron density distribution to be obtained with accurate refinement in the present work. Therefore, in further refinement calculations on our single-crystal XRD data, we adopted a procedure to distinguish the Ti^{3+} and Ti^{4+} cations in the crystal structure.

In these structure refinement calculations, X-ray scattering factors of the Ti^{3+} and Ti^{4+} cations^[24] and the O^{2-} anion^[25] were used instead of the X-ray scattering factors for neutral Ti and O atoms. At present, there is still no universally accepted X-ray

scattering factor for O^{2-} owing to its sensitivity to the local environment (i.e. the distribution of neighbouring positive charges), and in the present work we used the same scattering factor for all O^{2-} anions in the structure irrespective of whether they are located at 3-coordinate or 4-coordinate oxygen sites. At each Ti site, our refinement allowed occupancy by both Ti^{3+} and Ti^{4+} cations, with the total occupancy of Ti^{3+} and Ti^{4+} at each Ti site constrained to equal 1. Furthermore, the sum of the Ti^{3+} occupancies for the four independent Ti sites was constrained to equal 2 and the sum of the Ti^{4+} occupancies for the four independent Ti sites was constrained to equal 2, thus satisfying the formula Ti_4O_7 . The refined $\text{Ti}^{3+}/\text{Ti}^{4+}$ occupancies converged after a few cycles of refinement (the same refined occupancies were obtained irrespective of the initial values) and the quality of fit to the data (R_1 index) was very similar for the datasets at each temperature. The final spatial distribution of the Ti^{3+} and Ti^{4+} cations on the Ti sites, determined from our refinement strategy, is given in Table 2 and a graphical representation is shown in Figure 5.

Table 2. Occupancies of the Ti^{3+} and Ti^{4+} cations at each Ti site (denoted Ti1, Ti2, Ti3 and Ti4) in the crystal structure of Ti_4O_7 , refined from our single-crystal XRD data using independent scattering factors for the Ti^{3+} and Ti^{4+} cations.

T/K	Occupancy	Ti1	Ti2	Ti3	Ti4
298	Ti^{3+}	0.39(2)	0.42(2)	0.61(2)	0.59(2)
	Ti^{4+}	0.61(2)	0.58(2)	0.39(2)	0.41(2)
145	Ti^{3+}	0.40(3)	0.45(3)	0.60(3)	0.55(3)
	Ti^{4+}	0.60(3)	0.55(3)	0.40(3)	0.45(3)
98	Ti^{3+}	0.49(2)	0.30(2)	0.70(3)	0.51(3)
	Ti^{4+}	0.51(2)	0.70(2)	0.30(3)	0.49(3)

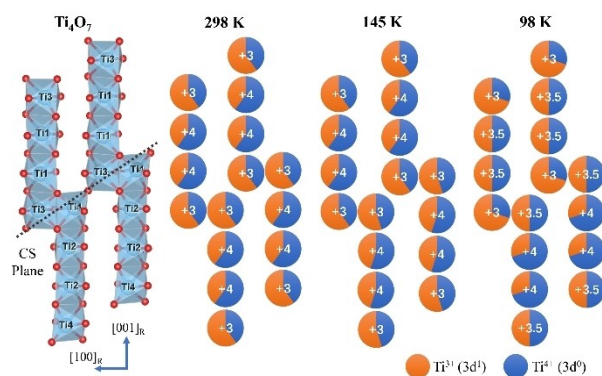


Figure 5. Representation of the distribution of Ti^{3+} and Ti^{4+} cations at each Ti site in the crystal structure of Ti_4O_7 , viewed along $[010]_{\text{R}}$, at three different temperatures, determined from the $\text{Ti}^{3+}/\text{Ti}^{4+}$ occupancies in Table 2. The Ti sites are labelled as either: +4 (if the occupancy of Ti^{4+} is higher than the occupancy of Ti^{3+} by an amount greater than the esds in the refined occupancies), +3 (if the occupancy of Ti^{3+} is higher than the occupancy of Ti^{4+} by an amount greater than the esds in the refined occupancies), or +3.5 (if the difference between the occupancies of Ti^{3+} and Ti^{4+} is less than the esds in the refined occupancies). The relative areas of the orange and blue regions representing each Ti site indicate the actual relative occupancies of Ti^{3+} and Ti^{4+} respectively.

To show each independent Ti site and the connection between TiO_6 octahedra, the structure is viewed along the $[010]_R$ direction in Figure 5, allowing the rutile blocks (edge-sharing octahedra Ti1 and Ti2) and corundum blocks (face-sharing octahedra Ti3 and Ti4) to be observed clearly. At 298 K, the Ti^{3+} ($3d^1$) cations are preferentially located (occupancy *ca.* 0.6) on the Ti3 and Ti4 sites, while the Ti^{4+} ($3d^0$) cations are preferentially located on the Ti1 and Ti2 sites (in contrast, previous studies^[11] proposed that the Ti^{3+} and Ti^{4+} cations are homogeneously distributed at all Ti sites in the high-temperature phase). At 145 K, there is a slight change in $\text{Ti}^{3+}/\text{Ti}^{4+}$ occupancies corresponding to a small amount of *d* electron transfer from the Ti4 site (increased Ti^{4+} occupancy) to the Ti2 site (increased Ti^{3+} occupancy). On decreasing temperature to 100 K, the *d* electron population on the Ti3 and Ti1 sites increases (increased Ti^{3+} occupancy) relative to the Ti4 and Ti2 sites (increased Ti^{4+} occupancy). These results are in broad agreement with the *d* electron transfer associated with the phase transitions in Ti_4O_7 reported previously,^[23] but yield more direct insights concerning the detailed distribution of the *d* electrons in each phase of Ti_4O_7 .

Our refinement of the $\text{Ti}^{3+}/\text{Ti}^{4+}$ cation occupancies in the Ti_4O_7 structure represents a first step towards a more comprehensive structural understanding of this material through combined analysis of high-quality single-crystal XRD data and 3D-ED data, which will lead to precise determination of the electron density and electrostatic potential distributions, respectively.

(b) Electron Diffraction: Several 3D-ED datasets were recorded for crystals of sub-micrometre size, and the bright field image of a Ti_4O_7 crystal is shown in Figure 6a. Figures 6b–d show projections of the reconstructed reciprocal lattice of Ti_4O_7 along the $[100]_M$, $[010]_M$ and $[001]_M$ directions, respectively, giving unit cell parameters: $a = 5.57 \text{ \AA}$, $b = 6.91 \text{ \AA}$, $c = 7.12 \text{ \AA}$; $\alpha = 64.97^\circ$, $\beta = 71.96^\circ$, $\gamma = 76.00^\circ$, $V = 234.13 \text{ \AA}^3$. The fact that there is no extinction of reflections is consistent with a primitive triclinic system (space group $P1$ or $P\bar{1}$). All 3D-ED datasets show resolution higher than 0.9 \AA (even higher resolution could be achieved using a smaller camera length). As the completeness of each dataset is less than 60%, three datasets were merged to give improved completeness (Table S1) of 97.55% (resolution, 1.0 \AA). Structure solution was carried out from the 3D-ED data using direct methods in the *SIR2014* software,^[27] giving a structure (Figure S4) in very good agreement with the structure determined from our single-crystal XRD data.

We note that the atomic scattering factor for electrons is much more sensitive to the valence/conduction electron distribution than the atomic scattering factor for X-rays, especially for reflections in the range $q < 1 \text{ \AA}^{-1}$, where $q = (4\pi \sin \theta)/\lambda$.^[28] Fortunately, the Andersson-Magnéli phases give many superlattice reflections in this *q*-range. Our precise ED intensity measurements for the superlattice reflections will commence soon.

(c) Physical properties (electrical conductivity and magnetic susceptibility): The temperature dependence of resistance *R* and magnetic susceptibility χ of a Ti_4O_7 single crystal is shown in Figure 7. From Figure 7a, the material shows metallic

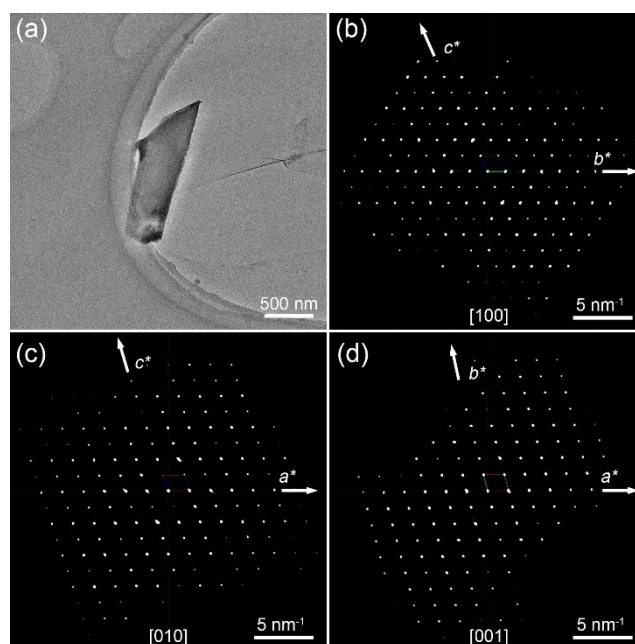


Figure 6. (a) Bright field image of a Ti_4O_7 crystal. Projections of reconstructed 3D-ED intensity distribution obtained from Ti_4O_7 along $[100]_M$, $[010]_M$ and $[001]_M$ directions, respectively, in (b), (c) and (d).

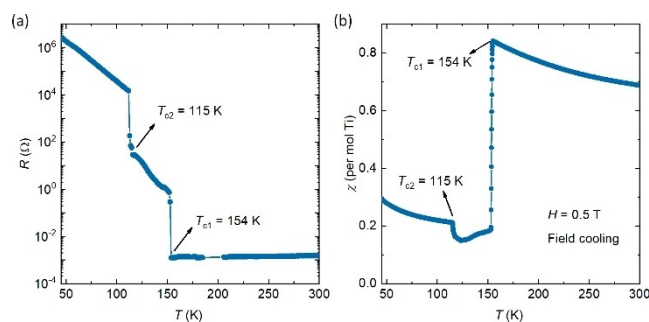


Figure 7. Physical properties of Ti_4O_7 single crystals: (a) temperature dependence of resistance, and (b) temperature dependence of magnetic susceptibility, measured with a 0.5 T field.

behaviour in the high temperature region and undergoes two transitions (MIT) on decreasing temperature from room temperature to 50 K, namely a metal-semiconductor transition at $T_{c1} \approx 154 \text{ K}$ and a semiconductor-semiconductor transition at $T_{c2} \approx 115 \text{ K}$, consistent with a previous report on Ti_4O_7 .^[15] Further cooling drives the sample to more insulator-like behaviour with considerably higher resistance (in the $\text{M}\Omega$ regime), beyond the measuring limit of the instrument. We note that the transition region is rather sharp, indicating the high quality of the single crystal.

Magnetic susceptibility results (Figure 7b) also show two almost identical transitions as a function of temperature: in the field cooling measurement (field, 0.5 T), the crystal transforms from paramagnetic to antiferromagnetic at the Néel temper-

ature $T_{c1} \approx 154$ K, in agreement with previous results.^[29,30] The second transition is relatively weak with critical temperature $T_{c2} \approx 115$ K, before the paramagnetic-like background increases significantly at lower temperature. We note that the second transition was not observed in previous results.^[29,30] Such divergence may be attributed to a lower density of data points near T_{c2} or poorer crystal quality in the earlier studies. However, we note that the magnetic transition is in good agreement with the transport transition at T_{c2} , for which the electronic states should be modified significantly, so the observation of a magnetic transition is not surprising.

For the mechanism of the two-step phase transition, it is essential to understand the crystal structure and particularly the Ti valence in the Andersson-Magnéli phase. Based on our crystallographic analysis of Ti_4O_7 at 298 K, 145 K and 98 K, the lattice parameters are significantly different in the three different phases (Table 1). Hard X-ray photoemission spectroscopy demonstrated a clear metallic Fermi edge and mixed valence of Ti above T_{c1} and a Mott insulating gap of ~ 100 meV below T_{c2} , with a pseudogap coexisting with remnant coherent states between T_{c1} and T_{c2} .^[13] The dramatically different band structure is basically attributed to localization of the $3d$ electrons of Ti in the $Ti^{3+}-Ti^{4+}$ pairs, which are stabilized by bipolaron formation,^[30] accordant with our analysis on the spatial distribution of Ti^{3+} and Ti^{4+} cations in Figure 5.

Concluding Remarks

In conclusion, we have reported a comprehensive examination of the Andersson-Magnéli phases Ti_nO_{2n-1} ($n = 4-8$), combining results from single-crystal XRD and electron microscopy to confirm the shearing structure derived from rutile TiO_2 in both micro-crystals and nano-crystals. The distribution of Ti^{3+} and Ti^{4+} cations in Ti_4O_7 , established from refinement of single-crystal XRD data (using X-ray scattering factors for Ti^{3+} , Ti^{4+} and O^{2-} ions), provides more detailed information on the valence states and d -electron distribution. HR-STEM images reveal all atoms in the structure, and also reveal variation in the region of the shear planes, which cannot be obtained from the average structural information derived from single-crystal XRD data. Electrical conductivity and magnetic susceptibility of a high-quality single crystal are also reported.

While the Andersson-Magnéli phases have been subjected to detailed study and characterization since the seminal work over 50 years ago discussed in the Introduction, there are still many deeper insights to be discovered about this fascinating family of materials. In the present day, we have access to a wide range of more powerful experimental and computational techniques as well as methods for preparation of samples of higher crystalline quality, which creates exciting opportunities to establish significantly more accurate knowledge and significantly more profound understanding of the Andersson-Magnéli phases in the years to come. An important aim of our future research on these materials is to move beyond "classical" descriptions in terms of the distributions of discrete Ti^{3+} , Ti^{4+} and O^{2-} ions, and instead to develop descriptions based on

precise electron density distributions, established from single-crystal XRD, state-of-the-art electron-beam techniques and complementary computational approaches.

Experimental Section

Synthesis: A high-quality single crystal of Ti_4O_7 was prepared as follows. TiO_2 and Ti were mixed in a 7:1 molar ratio, ground together, and pressed into rods, which were further sintered at 1000°C for 24 hr in an evacuated sealed quartz tube. The Ti_4O_7 single crystal was grown using the calcined rods by the optical floating-zone technique in pure argon atmosphere at growth rate 8–10 mm/hr. A high-quality Ti_4O_7 single crystal was obtained only at a seed rod rotation rate of 35 rpm.^[15]

Sample 1 and sample 2 were prepared by melting a mixture of pure metallic Ti powder and rutile TiO_2 powder by arc under argon protection. Different amounts of TiO_2 and Ti powders were mixed under stirring for 30 min, then pellets ($\Phi 8$, 0.15 g) were made by dry-pressing at 30 MPa for 1 min. Arc melting was conducted in the arc melting furnace (MAM 1, Johanna Otto GmbH, Germany) in the Department of Materials and Environmental Chemistry, Arrhenius Laboratory, Stockholm University, Sweden. After pumping and flushing three times, the chamber was filled with argon at standard atmospheric pressure and the pellets were melted by arc five times.

Scanning transmission electron microscopy and electron diffraction: Pieces scraped from the original bulk sample were crushed in a mortar for 15–20 min, then dispersed with ethanol and dripped onto holy-carbon supported films.

(a) **HR-STEM:** High resolution STEM images were recorded on a Scanning/Transmission Electron Microscope (S/TEM) JEM-Grand ARM 300F equipped with double spherical aberration (Cs) correctors, ADF/BF/SAAF detectors, and Electron Energy Loss Spectrometer with K2 camera and GIF spectrometer. Spatial resolution in STEM mode was down to 0.59 \AA at 300 kV, allowing characterization at the atomic level. With a $30 \mu\text{m}$ condenser lens aperture, the convergence angle was 24 mrad and the probe current was reduced to 15.9 pA to reduce the e^- beam irradiation. With a camera length of 30 cm, the collection angle of ADF images was 24 mrad to 131 mrad. The energy resolution of EELS was 1 eV in counting mode with a dispersion of 0.5 eV/channel. With a camera length of 2 cm, the collection semi-angle of the EEL spectrum was around 78 mrad. These parameters are set for least beam damage in the CS planes of the samples and a relatively good signal-to-noise ratio was obtained.

(b) **3D-ED:** A 200 kV Transmission Electron Microscope (TEM) JEM-2100Plus equipped with a TVIPS (XF416) CMOS camera was used for 3D-ED data collection. A high tilt sample holder (JEOL, Model 21010) was used to collect data at room temperature. 3D-ED data were collected in continuous mode with only goniometer rotation and with the camera operating in video mode. During data collection, electron diffraction patterns were recorded in selected area electron diffraction (SAED) mode with an aperture diameter of $2 \mu\text{m}$. Data collection parameters were optimized as: camera length, 80 cm; spot size, 5; exposure time, 0.2 s; averaged tilt step, 0.0751° . The whole tilt range of all data was ca. $100^\circ-115^\circ$. All recorded datasets were processed using EDT-Process software.^[31]

(c) **Single-crystal XRD:** Single-crystal XRD experiments were carried out on a single crystal of Ti_4O_7 ($31.0 \times 15.0 \times 12.5 \mu\text{m}^3$) at three temperatures using $\text{MoK}\alpha$ radiation ($\lambda = 0.71073 \text{ \AA}$). Measurements at 298 K and 98 K were carried out on a Rigaku XtaLAB Synergy Custom equipped with a rotating anode generator (FR-X: voltage, 45 kV; current, 66 mA). The measurement at 145 K was collected

using a Rigaku XtaLAB Synergy-S equipped with microfocus sealed tube with a mirror (PhotonJet-S: voltage, 50 kV; current, 1 mA). In each case, the detector was a hybrid photon counting detector (HyPix-6000HE: pixel size, $100 \times 100 \mu\text{m}^2$; active area, $77.5 \times 80.3 \text{ mm}^2$). The diffraction data were processed using CrysAlis^{Pro}.^[32]

(d) Electrical conductivity and magnetic susceptibility measurements: Electrical resistance of single crystals was measured on a polished fresh surface by the standard four-terminal method in the physical property measurement system (PPMS-14T) from Quantum Design. The maximum current applied before the crystal became insulating was 1 mA. Magnetic susceptibility of the single crystal was measured under a field of 0.5 T in the magnetic property measurement system (MPMS3) from Quantum Design. In the susceptibility measurement, the sample (mass, 12.8 mg) was attached to the quartz holder with GE-varnish and measured in DC mode.

Acknowledgements

We have learned from Swedish scientists through prolonged scientific interactions on titanium oxides, nano-porous crystals, differential geometry and complex inorganic crystals. One author (OT) received training in how to interact with people and how to run a research unit in a fair and open way, with self-introspective spirit, from Sven Lidin. Thank you Sven for your continuous encouragements. Prof. Jihong Yu is acknowledged for encouragement to JL, who is staying at ShanghaiTech University as an exchange student. We acknowledge Drs Daniel Eklöf, Mirva Eriksson and Yuan Zhong at MMK, Stockholm University and Drs Lu Song and Li Hezhen at the School of Materials Science and Engineering, Tsinghua University, for sample preparation. Support from ShanghaiTech University and the Centre for High-resolution Electron Microscopy (ChEM) through EM-19430216 and the National Natural Science Foundation of China (No. 61771234) are acknowledged.

Keywords: Andersson-Magnéli Phases · Scanning Transmission Electron Microscopy · Single Crystal X-ray Diffraction · Phase Transitions · Mixed Valence Materials

- [1] P. B. Hirsch, A. Howie, R. B. Nicholson, D. W. Pashley, M. J. Whelan, *Electron Microscopy of Thin Crystals*, London Butterworths, Great Britain, 1965.
- [2] F. A. Kröger, M. S. Seltzer, R. I. Jaffee, *Defects and Transport in Oxides*, Springer, US, 1974.
- [3] A. Brown, *X-Ray Powder Diffraction with Guinier-Hägg Focusing Camera*, Aktiebolaget Atomenergi, Sweden, 1970.

- [4] A. Magnéli, *J. Appl. Crystallogr.* **1987**, *20*, 1–2.
- [5] S. Andersson, B. Collen, U. Kuylenstierna, A. Magnéli, *Acta Chem. Scand.* **1957**, *11*, 1641–1652.
- [6] S. Andersson, *Acta Chem. Scand.* **1960**, *14*, 1161–1172.
- [7] O. Terasaki, D. Watanabe, *Jpn. J. Appl. Phys.* **1971**, *10*, 292–303.
- [8] L. A. Bursill, B. G. Hyde, O. Terasaki, D. Watanabe, *Phil. Mag.* **1969**, *20*, 347–359.
- [9] L. N. Mulay, W. J. Danley, *J. Appl. Phys.* **1970**, *41*, 877–879.
- [10] R. F. Bartholomew, D. R. Frankl, *Phys. Rev.* **1969**, *187*, 828–833.
- [11] M. Marezio, D. B. McWhan, P. D. Dernier, J. P. Remeika, *J. Solid State Chem.* **1973**, *6*, 213–221.
- [12] H. Ueda, K. Kitazawa, H. Takagi, T. Matsumoto, *J. Phys. Soc. Jpn.* **2002**, *71*, 1506–1510.
- [13] M. Taguchi, A. Chainani, M. Matsunami, *Phys. Rev. Lett.* **2010**, *104*, 106401.
- [14] K. Yoshimatsu, O. Sakata, A. Ohtomo, *Sci. Rep.* **2017**, *7*, 12544.
- [15] Q. Liu, Z. Liu, X. Zhou, Z. Liu, M. Huo, X. Wang, Y. Sui, *Cryst. Growth Des.* **2019**, *19*, 730–736.
- [16] A. A. Lafarga, L. R. González, M. Parras, *Chem. Rec.* **2018**, *18*, 1105–1113.
- [17] X. Tao, J. Wang, Z. Ying, *Nano Lett.* **2014**, *14*, 5288–5294.
- [18] S. Harada, K. Tanaka, H. Inui, *J. Appl. Phys.* **2010**, *108*, 083703.
- [19] E. Stoyanov, F. Langenhorst, G. S. Neumann, *Am. Mineral.* **2007**, *92*, 577–586.
- [20] G. M. Sheldrick, *Acta Crystallogr.* **2015**, *A71*, 3–8.
- [21] G. M. Sheldrick, *Acta Crystallogr.* **2015**, *C71*, 3–8.
- [22] O. V. Dolomanov, L. J. Bourhis, R. J. Gildea, J. A. K. Howard, H. Puschmann, *J. Appl. Crystallogr.* **2009**, *42*, 339–341.
- [23] C. Schlenker, M. Marezio, *Philos. Mag. B* **1980**, *42*, 453–472.
- [24] D. T. Cromer, J. B. Mann, *Acta Crystallogr.* **1968**, *A24*, 321–324.
- [25] E. Hovestreydt, *Acta Crystallogr.* **1983**, *A39*, 268–269.
- [26] M. C. Burla, R. Caliendo, B. Carrozzini, G. L. Casciarano, C. Cuocci, C. Giacovazzo, M. Mallamo, A. Mazzzone, G. Polidori, *J. Appl. Crystallogr.* **2015**, *48*, 306–309.
- [27] K. Momma, F. Izumi, *J. Appl. Crystallogr.* **2011**, *44*, 1272–1276.
- [28] Y. Ma, L. Han, Z. Liu, A. Mayoral, I. Diaz, P. Oleynikov, T. Ohsuna, Y. Han, M. Pan, Y. Zhu, Y. Sakamoto, S. Che, O. Terasaki, *Microscopy of Nanoporous Crystals. In: Springer Handbook of Microscopy* (Eds. P. W. Hawkes, J. C. H. Spence), p. 1391–1450. Springer Nature Switzerland AG **2019**.
- [29] L. K. Keys, L. N. Mulay, *Jpn. J. Appl. Phys.* **1967**, *6*, 122–123.
- [30] W. J. Danley, L. N. Mulay, *Mat. Res. Bull.* **1972**, *7*, 739–748.
- [31] S. Lakkis, C. Schlenker, B. K. Chakraverty, R. Buder, M. Marezio, *Phys. Rev. B* **1976**, *14*, 1429–1440.
- [32] M. Gemmi, P. Oleynikov, *Z. Kristallogr.* **2013**, *228*, 51–58.
- [33] T. Matsumoto, A. Yamano, T. Sato, J. D. Ferrara, F. J. White, M. Meyer, *J. Chem. Crystallogr.* **2020**, <https://doi.org/10.1007/s10870-020-00867-w>.

Manuscript received: October 31, 2020

Revised manuscript received: December 12, 2020

Accepted manuscript online: December 25, 2020